Measuring the impact of laser relative intensity noise on heterodyne interferometers using differential wavefront sensing

L. Wissel[1,2,*] M. Hewitson[3] and G. Heinzel[1,2]

[1]*Max Planck Institute for Gravitational Physics (Albert-Einstein-Institut), Hannover 30167, Germany*
[2]*Leibniz Universität Hannover, Hannover 30167, Germany*
[3]*European Space Technology Centre, European Space Agency, Keplerlaan 1, Noordwijk 2200 AG, The Netherlands*

Laser-intensity fluctuations cause undesired phase noise even in balanced heterodyne interferometers. However, in space missions in particular, such as LISA Pathfinder or LISA, direct measurements of these fluctuations at the relevant frequencies are often not available. Hence, it can be challenging to estimate their impact on the interference phase. To address this, we propose a new method for characterizing laser relative intensity noise (RIN) using differential wavefront sensing (DWS), with the latter being a well-established technique typically used for angular sensing and control. Unlike other methods, this approach does not require an additional reference interferometer and instead takes advantage of the inherent phase subtraction of DWS. This allows us to estimate the RIN value at the heterodyne frequency and its harmonic, relative to the sensor noise floor of the total measurement system. Moreover, it provides a strategy to identify the ideal set point for minimizing RIN couplings in DWS.

I. INTRODUCTION

Balanced heterodyne interferometers have been crucial instruments in highly sensitive displacement measurements, used in various applications, naturally including scientific space missions [1,2]. However, estimating laser-intensity fluctuations, also known as laser relative intensity noise (RIN) [3–5], has been a challenge in space missions such as LISA Pathfinder (LPF) [6,7]. RIN couples into the interference phase, causing undesirable phase noise that reduces the sensitivity in the high-precision measurements. To understand the overall sensitivity in flight, a direct RIN measurement covering all potential coupling frequencies would be necessary. However, this is impractical for space missions with limited data recording, processing, and transmission capabilities.

Differential wavefront sensing (DWS) is a technique widely used for angular sensing and control [8–11]. It holds potential as part of the solution to this issue. DWS measures the wavefront tilt differences between two interfering beams using quadrant photodiodes (QPDs). The wavefront tilt differences have a significant effect on the interference signal, and an effective measurement is provided through the phase distribution changes observed on the QPD segments by comparing the top-bottom and left-right quadrants. RIN appears as a correlated noise on all these quadrants.

DWS inherently includes a reference phase subtraction from the complementary quadrants, which provides the possibility to characterize RIN without requiring an additional reference interferometer for this purpose.

One effective methodology to exploit the DWS scheme involves the controlled tilting of wavefronts. This creates a phase shift between the correlated noise vectors on the quadrants, enabling the maximization of the RIN coupling in the phase readout. Once the RIN is effectuated into the phase readout, it becomes possible to estimate the quantity with reliable accuracy due to its common-mode rejection properties.

Exploring the DWS parameter space through a series of varying tilts allows for fitting the RIN models to the collected data, ascertaining the coupling strength and the intensity of the so-called 1*f*- and 2*f*-RIN components (described further in Sec. III). The procedure involves careful analysis of the collected data and its application to the developed RIN model.

We further look at a technique called "balanced detection," which can be adopted to suppress intensity noise by subtracting two π-shifted interferometer output ports.

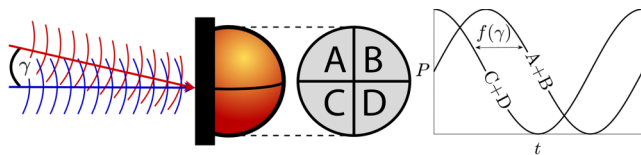*Contact author: lennart.wissel@aei.mpg.de

FIG. 1. Illustration of a heterodyne DWS measurement with two incoming wavefronts having an exemplary tilt angle γ in one spatial dimension. This translates to a phase difference between top and bottom segments of a QPD as visible in the corresponding power signals of the heterodyne beats.

Balanced detection is also beneficial for DWS because it suppresses the $1f$-RIN component, allowing a direct measurement of the impact of $2f$-RIN (which remains unaffected by balanced detection).

For reference, it is noted that a similar experiment (with longitudinal steps instead of angular tilts) has been performed in the past using common-mode subtraction properties of the longitudinal pathlength signal, where, in contrast to DWS, it is necessary make use of an additional, independent reference interferometer sharing the same correlated noise [5,12].

Overall, the methods presented here (based on findings in Refs. [6,7,13–17]) demonstrate how laser-intensity fluctuations can be estimated and mitigated to improve sensitivity and noise modeling using a typical DWS setup, as it is also planned for the future Laser Interferometer Space Antenna (LISA) mission.

II. DWS IN HETERODYNE INTERFEROMETERS

DWS is a technique to measure the tilt of an optical wavefront with high precision. In heterodyne interferometers, where the power on the photodiodes is oscillating at a frequency f_{het}, DWS is implemented by measuring averaged phase differences between two points on a wavefront, which correspond to the wavefront's tilt γ, as illustrated in Fig. 1. This is done by comparing phase measurements between segments of the QPDs. The different quadrant phases (q_A, q_B, q_C, q_D) are combined to form the well-known standard combinations

$$\phi^{\text{raw}} = \frac{(q_A + q_C) - (q_B + q_D)}{2}, \qquad (1)$$

$$\eta^{\text{raw}} = \frac{(q_A + q_B) - (q_C + q_D)}{2}. \qquad (2)$$

They correspond to the vertical and horizontal tilt angles between the wavefronts, with an advantageous magnification factor in the order of a few thousand, that depends on the geometrical beam properties (represented by $f(\gamma)$ in Fig. 1) [7,10,18].

The resulting α^{raw} (shorthand notation for either ϕ^{raw} or η^{raw}) can be calibrated to yield effective angles α (shorthand notation for either ϕ or η) of the physical object under test, for example a steering mirror, a free falling test mass, or a spacecraft telescope with a certain pointing, from which the beam is reflected. The linearity range of $f(\gamma)$ may effectively be in the order of a few hundred μrad around $\alpha = 0$ rad.

One advantage of DWS is that the pathlength difference between the two "interferometers" formed by the top/bottom and left/right quadrants, respectively, is very small. This effectively suppresses direct phase noises, such as frequency noise, and enhances the sensitivity to RIN in the experiments detailed in the following. However, this (using two quadrants each instead of four) comes at the cost of increasing the influence of uncorrelated readout noises by a factor of $\sqrt{2}$ in units of phase noise, compared with the longitudinal pathlength signal. This is due to an overall lower signal-to-noise ratio. In the longitudinal signal, all four quadrants are summed, and the DWS signals cancel due to symmetry.

III. RIN COUPLING IN DWS

Laser RIN r is defined as the fluctuations of the laser power δP normalized by the average beam power P,

$$r = \frac{\delta P}{P}, \qquad (3)$$

and is often expressed in units of an amplitude spectral density (ASD), referred to as $\tilde{r}$ [Hz$^{1/2}$]. By adding small subscripts ($r_{1,2}$, $P_{1,2}$, $\delta P_{1,2}$) the two interfering beams can be distinguished, since both contribute a phase error.

From previous publications [3–5,15,19] we know that RIN couples in a heterodyne interferometer via three separate mechanisms. First, from photon radiation pressure on movable reflective surfaces along the optical path, causing mainly longitudinal pathlength fluctuations, that subtract to a large extent in DWS. Second, the so-called $1f$-RIN coupling, which is causing phase noise depending of the RIN spectral density at the heterodyne frequency, $\tilde{r}(1f_{\text{het}})$, and, third, $2f$-RIN, which is causing phase noise from RIN at twice the heterodyne frequency, $\tilde{r}(2f_{\text{het}})$.

Therefore, the main effects that affect DWS originate from $1f$- and $2f$-RIN. Due to their correlation across quadrants the common mode rejection depends on the corresponding DWS angle α^{raw}.

The phase noise in either DWS angle can be described by the following equations (adapting Ref. [5] for DWS). If r_1 and r_2 are correlated with equal ASD ($\tilde{r}_1 = \tilde{r}_2 = \tilde{r}$), the equations in units of phase noise (representing components of $\tilde{\alpha}^{\text{raw}}$ in [rad Hz$^{-1/2}$]) are

$$\tilde{\alpha}_{1f}^{\text{raw}} = \frac{\sqrt{2}\,(P_1 + P_2)}{\sqrt{\eta_{\text{het}} P_1 P_2}}\,\tilde{r}(1f_{\text{het}})\left|\sin\left(\frac{\alpha^{\text{raw}}}{2}\right)\right|, \qquad (4)$$

$$\tilde{\alpha}_{2f}^{\text{raw}} = \sqrt{2}\tilde{r}(2f_{\text{het}})\,|\sin(\alpha^{\text{raw}})|, \qquad (5)$$
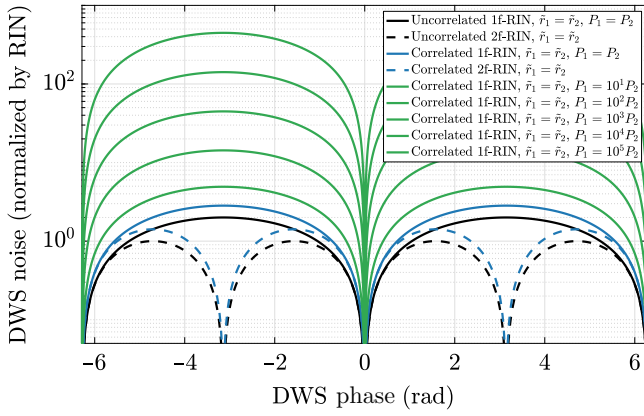
FIG. 2. Plot of the RIN coupling equations with the resulting phase error in DWS, normalized by the RIN value $\tilde{r}$. This plot is the basis of the experimental RIN characterization in this article. It shows the zeros for $1f$- and $2f$-RIN and the magnification of the coupling due to beam power mismatches (increasing noise for larger mismatches).

and if they are uncorrelated, for example from different lasers (but still with $\tilde{r}_1 \approx \tilde{r}_2 = \tilde{r}$), the coupling yields

$$\tilde{\alpha}_{1f,u}^{raw} = \sqrt{\frac{2\left(P_1^2 + P_2^2\right)}{\eta_{het}P_1P_2}}\,\tilde{r}\,(1f_{het})\left|\sin\left(\frac{\alpha^{raw}}{2}\right)\right|, \quad (6)$$

$$\tilde{\alpha}_{2f,u}^{raw} = \tilde{r}\,(2f_{het})\,|\sin(\alpha^{raw})|. \quad (7)$$

Here, η_{het} describes the heterodyne efficiency entering from the overlap integral of the interfering beams [18]. It reaches 1 for ideal alignment and degrades for imperfect overlap.

Figure 2 shows the normalized coupling strength based on the DWS phase for the various cases and includes power mismatches $P_{1,2}/P_{2,1}$ up to 10^5 for correlated RIN. By multiplying the y axis with the RIN ASD value one finds the resulting phase noise in $[\text{rad Hz}^{-1/2}]$. The maximum factor between correlated and uncorrelated DWS noise is given by

$$\left.\frac{\tilde{\alpha}_{1f}^{raw}}{\tilde{\alpha}_{1f,u}^{raw}}\right|_{max} = \left.\frac{P_1 + P_2}{\sqrt{P_1^2 + P_2^2}}\right|_{max} = \sqrt{2}, \quad \text{if } P_1 = P_2, \quad (8)$$

with the limit $\to 1$ if there is a large mismatch. Therefore, in the cases of beam-power mismatches, only the $1f$-RIN equation for correlated RIN is plotted.

The total noise in DWS for either ϕ^{raw} or η^{raw} (again using placeholder α^{raw}) is the squared sum of the $1f$- and the $2f$-RIN phase noise terms,

$$S_{RIN}^{1/2}\left(\tilde{r}, \alpha^{raw}\right) = \sqrt{\left(\tilde{\alpha}_{1f/,u}^{raw}\right)^2 + \left(\tilde{\alpha}_{2f/,u}^{raw}\right)^2}. \quad (9)$$

This requires to apply the correct equations for correlated or uncorrelated (subscript "u") RIN coupling depending on the experimental setup.

Regarding the $1f$-RIN terms it is important to note that these equations are only true if the beam powers are identical between the quadrants, which is naturally a good approximation for well-aligned Gaussian beams in their fundamental mode. However, wavefront tilts may introduce beam walks due to lever arm effects on the photodiode surface if no imaging optics are set up, as it was the case for LPF, but is different for LISA.

Overall, from the presented equations it follows that if the DWS readout is at 0 rad, the RIN coupling is minimal. This represents the most effective suppression strategy. However, the reverse is also true: if the RIN coupling is minimal, the raw DWS readout is around 0 rad. Therefore, by measuring the noise (as done in the experiments in this paper), and without knowledge of the DWS to physical test mass angle calibration factors, this allows us to find the minimum noise coupling. This could function as a cross-test if there has been a knowledge uncertainty, for example if only the calibrated data are available due to limited telemetry.

IV. BALANCED DETECTION

Balanced detection is a technique commonly used for improving measurement sensitivity and reducing noise.

Traditional interferometers use a single photodetector to measure the intensity of the interference pattern. In balanced detection, the interference pattern is split into two paths, and two separate photodetectors measure the intensities of the two paths. This typically involves a lossless recombination beam splitter, which implies a π phase shift between the two output ports due to energy conservation. The electrical signals from the photodetectors are then subtracted from each other. This technique helps in canceling out common-mode noise and unwanted background signals, while providing signal redundancy.

Assuming a signal s and a common, correlated noise (such as $1f$-RIN) n, the two ports conceptually measure $s + n$ (port A) and $-s + n$ (port B). Thus, balanced detection entails a calculation of the type $((s + n) - (-s + n))/2 = s$. The complete removal of the noise in the last step (or, rather, its efficiency) depends on equal amplitudes and phases of the noise vectors in both output ports.

Balanced detection reaches high suppression with ideal 50/50 beam splitters and equal electrical processing gains of each photodiode segment.

Overall, by subtracting the two detector outputs, balanced detection helps in improving the signal-to-noise ratio and effectively suppresses common noise sources such as laser-intensity noise from $1f$-RIN. However, $2f$-RIN cannot be removed, since it is subject to the same π phase shift as the signal [5].

V. OUR TESTBED: THE LISA PATHFINDER SPACE MISSION

The LPF mission was a precursor mission to LISA, which will detect and study gravitational waves in space. Launched in December 2015 by the European Space Agency (ESA), LPF successfully demonstrated the key technologies necessary for future implementation of LISA [20,21].

The mission's primary objective was to demonstrate the free fall of two test masses with sufficient low noise levels as needed for gravitational wave detection in LISA. LPF housed high-precision interferometers, tasked with meticulously monitoring the position and orientation changes of the test masses. These test masses, shielded from external influences, floated in a state of near-perfect free fall, isolated from any nongravitational forces.

The experiments discussed in this article were possible thanks to the excellent low-noise performance provided by the so-called optical metrology system (OMS) and the gravitational reference sensor (GRS), respectively.

On the one hand, the OMS hosted four laser interferometers that allowed the distance variations and changes in orientation between the two test masses (and between test mass 1 and the spacecraft) to be measured to very high precision; see Fig. 3. This enabled the detection of incredibly small changes in distance, with a residual sensor noise of $32.0^{+2.4}_{-1.7}\,\text{fm}/\sqrt{\text{Hz}}$ along x above 200 mHz and an angular sensitivity of approximately $100\,\text{prad}/\sqrt{\text{Hz}}$ in the ϕ and η DWS coordinates (as visible in Fig. 4; see also Ref. [7] for more details).

The OMS operated using a single Nd:YAG laser with a wavelength of 1064 nm. It worked by initially splitting this laser into two beams. Each beam's frequency was then adjusted by acousto-optical modulators, creating a difference frequency f_{het}, set to 1 kHz. Following these alterations, the beams were directed to the optical bench. Here, they followed a measurement path (red trace in Fig. 3) and a reference path (blue trace in Fig. 3) before their beat signals were detected at two output ports with QPDs, enabling balanced detection. The phase extraction occurred through the use of single-bin discrete Fourier transforms and phase tracking algorithms.

The measurements from the OMS were used by the spacecraft's dragfree and attitude control system (DFACS) to adjust the spacecraft's position and maintain it in a dragfree orbit around the test masses. This ensured that the test masses remained in a perfect free-fall state, isolated from nongravitational forces.

On the other hand, the GRS provided sophisticated electrostatic sensing and actuation capabilities, which were also integral to the mission's DFACS [22].

The electrostatic sensing capability of the GRS involved measuring the position and orientation of the test masses relative to their housings. This was achieved by detecting
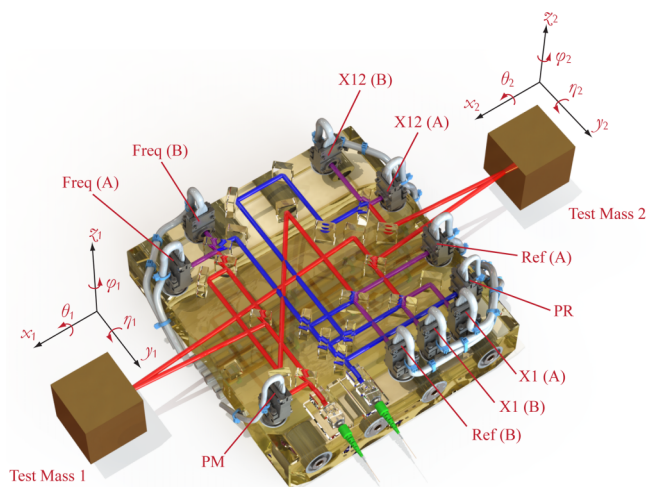

FIG. 3. Illustration of the LPF optical bench with the four interferometers and the distances and angles measured by the OMS. For the experiments discussed in this article, one or both test masses were tilted in the ϕ, η plane (please note that the test mass angles are labeled ϕ in this article compared with φ in this rendering). The photodiodes are named by interferometer and are labeled (A) and (B) for the two output ports of each recombination beam splitter. PM, power measurement diode for the measurement beam; PR, power measurement diode for the reference beam. Reprinted with permission from Ref. [6].

the capacitance changes between the test masses and surrounding electrodes. These measurements allowed the DFACS to determine the exact position of each test mass in six degrees of freedom (three translational and three rotational, including the three degrees of freedom that were sensed in parallel by the more sensitive OMS).

The actuation capabilities were used to apply forces and torques to the test masses without physical contact, using electrostatic forces. This was done by applying voltage to the electrodes surrounding the test masses. By carefully controlling these voltages, the DFACS could adjust the position and orientation of the test masses, ensuring they remained in a state of pure free-fall and perfectly centered within their housings.

Using the capabilities of the GRS and OMS together, we performed the experiments by tilting the test masses to a number of different set points via the GRS actuation, and analyzed the effects of RIN in DWS, as explained in the next section.

VI. EXPERIMENTS

In particular, two experiments from the LPF mission can be used to investigate the RIN-to-DWS coupling. The basic principle in both of them consisted of commanding a set of angular test mass orientations via the electrostatic controller to rotate test masses 1 and 2 around their y and z axes, and calculate the resulting amplitude spectral noise
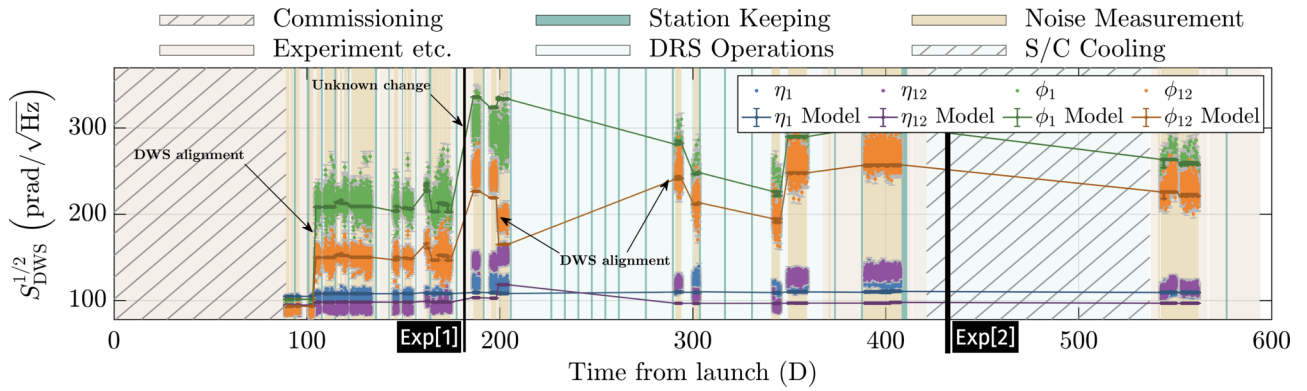
FIG. 4. Overview of the DWS sensitivity measurements for the full mission, scaled to test mass angles. Most of the noise changes can be attributed to RIN coupling. The two experiments addressed in this article have been marked. Modified with permission from Ref. [7]; further details can be found there.

density each time. LPF has proven to be quiet enough to reach a quasiflat, sensor noise dominated sensitivity at the high-frequency range in the angular test mass readout above about 1 Hz [6,7], that is sensitive to the RIN coupling described previously.

Motivation for these investigations arose from observations during the mission: the test mass alignment along ϕ_1, η_1, ϕ_2, and η_2 (see Fig. 3) had shown a varying noise floor (at frequencies > 1 Hz affected by RIN) for each of a set of static angular set points that were originally applied to reduce another noise, the so-called tilt-to-length coupling (at lower frequencies 20 mHz to 200 mHz) [7,23]. This is indicated by the "DWS alignment" annotations in Fig. 4, which shows the changing DWS noise performance during the mission under nominal operating conditions. In this plot, the two experiments discussed here are highlighted. It can be seen that they were performed under different operating conditions. The first happened during a period of an unknown increase in the overall noise, whereas the second experiment was run during a phase of spacecraft cooling, that reduced the temperatures from about 22 to 11 °C.

The RIN coupling was found to be the cause of most of the changing behavior (above 1 Hz) over the course of the mission. It became obvious that its influence on DWS may be used to characterize the strength and validate an noise optimized operating point. It should be noted that no direct RIN measurement at kHz frequencies was available onboard for telemetry, even though there was an analog power stabilization loop active.

A. DWS experiment 1

The first experiment was performed during the main mission when the exact RIN to DWS coupling was still unknown. It was not optimized for the RIN characterization, but it still contains valuable data and was therefore included in this article.

For the tilts selected in this experiment, only test mass 2 was chosen because of its closer position to the photodiodes, minimizing any resulting beam-walk on the surface of the quadrants, and because it is influencing the differential interferometer, which is less susceptible to environmental disturbances.

To perform this investigation, a time slot of 24 h was available, starting from 2016-06-02 08:30 UTC. The static tilts performed previously (to reduce tilt-to-length coupling) showed that a test mass needs roughly 30 min to stabilize after an actuation command is issued. With 15 min measurement time afterward, it limited the number of slews to 30 while still allowing a transition back to nominal test mass orientation after the last measurement point. The plot of this experiment is given in Fig. 5, see also Ref. [16].

The investigation procedure consisted of one actuation command per step. It required that during the experiment, the spacecraft was in DFACS mode SCI1.2 (high-resolution sensing, low actuation authority on the electrostatic controllers) and that the following sequence was repeated for all set points: (1) issue the actuation command from the current set point to the next set point; (2) wait
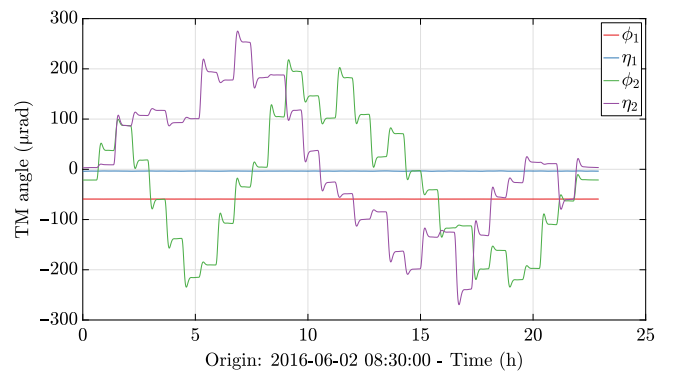

FIG. 5. Time series of the first experiment in units of test mass angles.

30 min for the test mass to stabilize; (3) measure the DWS noise for 15 min.

In this first experiment, the tilts were limited to a parameter space of $\pm 250\,\mu$rad for the test mass 2 angles.

During the noise measurement the system was kept in its current state without any other commanding, assuring stable measurement conditions.

B. DWS experiment 2

An enhanced version of the first DWS experiment was planned during the mission extension, which aimed to increase the test mass 2 tilts to explore a more extensive phase space while reducing the beam walk by simultaneously actuating test mass 1. It also included measurements without balanced detection.

The commanded slews followed a stepwise scheme, covering a range of approximately $-600\,\mu$rad to $600\,\mu$rad for test mass 2 in ϕ_2, η_2. Similar to the first experiment, the noise was measured at each set point. However, after a few minutes at each set point the B side of the phasemeter was "masked." This procedure effectively turned off balanced detection, as the entire second output port of the interferometer was deactivated. Subsequently, the noise was measured in this new "unbalanced" configuration before unmasking the B side again and proceeding to the next set point, where the process was repeated. Figures 6 and 7 show an overview of the experiment scaled to test mass tilts and the resulting contrast. Observations show a consistent minor overshoot prior to stabilizing at a new set point, aligning with expectations based on prior experiments. In limited instances, for brief durations, four data channels were acquired at a sampling frequency of 100 Hz through the so-called interferometric data log for diagnostic objectives. The moments when this data was collected have been masked due to the introduction of transients in certain channels by the process.

The experiment commenced on February 6, 2017, at 23:06 and continued for approximately 48 h. However, due to a failure in a preceding experiment, test mass 2 was not
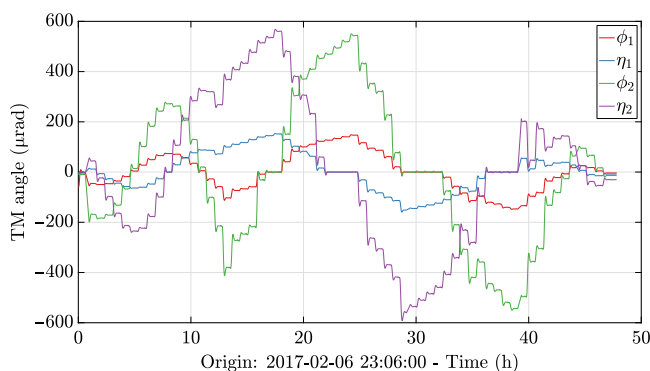
at its zero position, but remained at a longitudinal offset of 275 nm.

This second experiment was conducted during the cooling phase of the spacecraft and, therefore, potentially influenced by different conditions. However, the laser unit itself was only a few °C lower compared with before cooldown (still above 20 °C) and the effect is hard to quantify. It was likely that the optical beam paths have changed due to thermomechanical stresses leading to a small bending of the optical bench, which was compensated for by the electrostatic controllers, keeping the DWS readouts stable [24].

C. Description of the data

During the experiments, the sampling frequency of the data telemetered to Earth was set to 10 Hz and contained the interferometric DWS channels, optical powers and contrasts per interferometer averaged across both output ports, as well as housekeeping data.

The nature of the data acquisition process imposed certain limitations. Consequently, only the data that had undergone a range of steps was available for analysis. First, a single-bin discrete Fourier transform was applied, which already included a downsampling step from 50 kHz to 100 Hz. A subsequent downsampling step reduced the frequency to 10 Hz using a moving average filter. Finally, the data underwent DWS processing before it was prepared for telemetry. The second downsampling process was necessary to reduce the data transmission rate to ground. However, it is worth noting that downsampling may introduce aliasing effects in the data, potentially affecting the final results of the experiment. In addition, no individual quadrant data were available.

The processing that took place onboard resulted in DWS signals from the unique quadrant phases of the so-called X1 interferometer (ϕ_1^{raw}, η_1^{raw}, denoting raw wavefront angles from test mass 1 relative to the optical bench) and the X12 interferometer (ϕ_{12}^{raw}, η_{12}^{raw}, indicating differential wavefront angles), as detailed in Eq. (1). Utilizing a linear combination and calibration coefficients derived from before flight, these signals were processed into physical test mass angles $\phi_1, \eta_1, \phi_2, \eta_2$ with respect to the onground calibration. For the purpose of our evaluation in this article, these quantities have been inverted again during post-processing, as the direct dependence of RIN coupling relies on the "raw" DWS data.

Due to the demanding schedule of mission activities and other experiments, it was only possible to run each of the experiments once. The duration of each segment was only in the order of 7 min, thus reducing the amount of time segments available for averaging.

FIG. 6. Time series of the second experiment in units of test mass angles. Modified with permission from Ref. [17].

D. Noise model

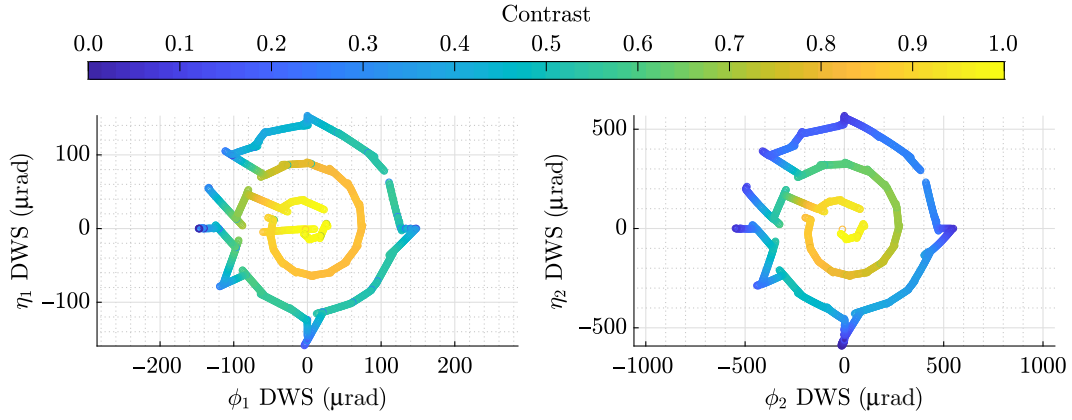The noise model used here is a simplified version of the noise model presented in Fig. 4, (see Ref. [7,

FIG. 7. Overview of the second experiment. First test mass is shown on the left, second test mass with larger tilts on the right in units of test mass tilts. Note that some segments have been masked out due to onboard packet switching causing transients. Modified with permission from Ref. [17].

equations (9)–(26)]), since we do not need to propagate the DWS measurements through the test mass angle linear combinations. It only contains the $2f$-RIN coupling (dominant RIN term in LPF) from Eq. (4) and additive readout noises such as shot noise and phasemeter noise (mainly depending on analog-to-digital convertor (ADC) quantization noise $\tilde{I}_{ADC}$). The readout noises scale reciprocally with the contrast (c_i for each interferometer), and the shot noise that also depends on the average power Σ_i per interferometer. Hence, the total noise model for each DWS channel is (either X1 for ϕ_1, η_1 or X12 for ϕ_{12}, η_{12})

$$S_{DWS,X1} = S_{RIN}\left(\tilde{r}, \{\phi_1^{raw}, \eta_1^{raw}\}\right) + S_{Phasemeter}\left(c_1, \tilde{I}_{ADC}\right)$$
$$+ S_{Shot\ noise}\left(c_1, \Sigma_1\right), \tag{10}$$

$$S_{DWS,X12} = S_{RIN}\left(\tilde{r}, \{\phi_{12}^{raw}, \eta_{12}^{raw}\}\right) + S_{Phasemeter}\left(c_{12}, \tilde{I}_{ADC}\right)$$
$$+ S_{Shot\ noise}\left(c_{12}, \Sigma_{12}\right). \tag{11}$$

The fit in the data analysis is then using two free parameters which are not directly known: $\tilde{r}$ and $\tilde{I}_{ADC}$. The other parameters are known from telemetry.

This noise model describes the pseudoflat sensor noise floor above 1 Hz, where no real angular motion is visible.

It should be noted that it is only due to the high-sensitivity and low-noise configuration of LPF, well below requirements, that this experiment was possible.

E. Data analysis

Since only one laser was used, the equations for correlated RIN between the two interfering beams are used. The acousto-optic modulators may introduce uncorrelated RIN between the two beams, but the influence is unknown and assumed negligible here.

By design, $r(t)$ appears correlated on all quadrants. Therefore, all DWS channels can be jointly analyzed. The

raw phases η_1^{raw}, ϕ_1^{raw} (from X1), and η_{12}^{raw}, ϕ_{12}^{raw} (from X12) were measured onboard. Only the calibrated test mass angles η_1, ϕ_1, η_2, ϕ_2 from linear combinations of the raw phases were available as telemetry. To use these in our model, the linear combinations are reversed as described previously. Then, all raw phases can be plotted on the same x axis.

For the subsequent analysis, stable segments were chosen based on a threshold criterion permitting the contrast (for X1 and X12 individually) to vary by less than $0.2\,\%\,\mathrm{s}^{-1}$. These segments were subsequently divided into periods of balanced detection (configuration for experiment 1 and 2) and unbalanced detection (only applicable for experiment 2).

For each individual segment of the first experiment, the LPSD is shown in Fig. 8. It can be seen that the noise floor above 1 Hz is relatively flat and depends on the angular set point. Further, some spectral lines are present. The exact coupling of the $n \cdot 1$ Hz components is unknown [12], but those spectral components are likely caused by the pulse-per-second timer and are masked out before averaging. The second experiment has very similar spectral densities per segment (not shown here).

To investigate the coupling per tilt angle, we calculate the power spectral density (PSD) for each tilt using 50 % overlapping Blackmann-Harris-92 (BH92) windows with 30 averages. Only every fourth bin is retained to avoid correlations between neighboring bins [27]. At 2 Hz the center bin and two surrounding bins are masked to remove the influence of onboard 1 Hz harmonics. Afterward, the spectrum is averaged. To allow for comparison with (Fig. 4, [7]), the same frequency range of 1.2 Hz to 2.8 Hz has been chosen.

However, it should be noted that not all segments show a particular white noise floor. They have slightly different gradients on them, as visible in Fig. 8. It can be seen that higher noise levels associated with larger test mass tilts
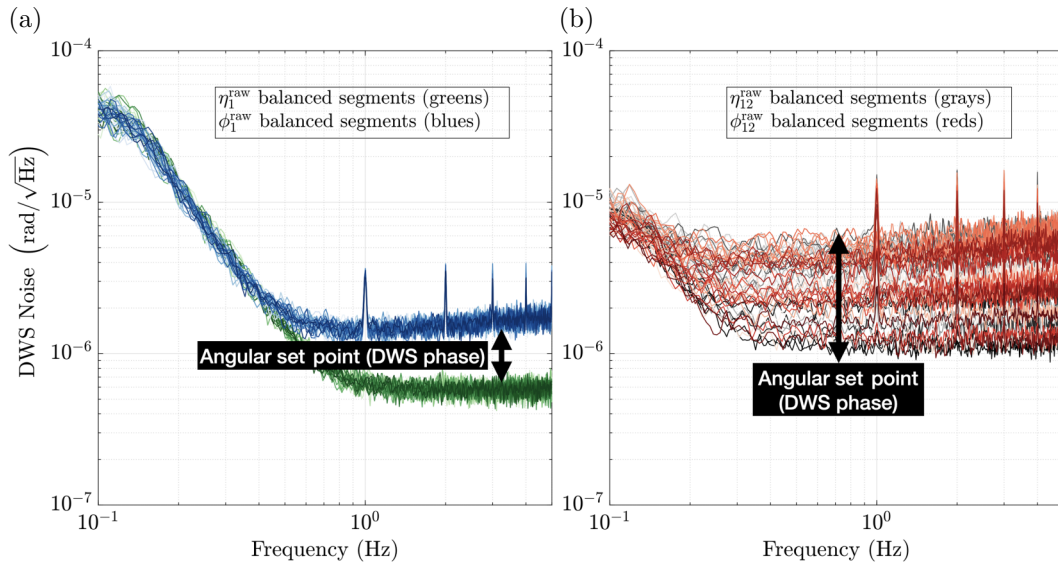
FIG. 8. First DWS experiment with ASDs for each angular set point. (a) X1 interferometer raw DWS angles of test mass 1. (b) X12 interferometer raw DWS differential angles between test mass 1 and 2. The amount of noise depends on the angular set point, which was constant (but not zero) for test mass 1 angles and varying for test mass 2. In the second experiment (not shown in this plot) both test masses were actuated. Figure produced using the logarithmic-frequency-axis power spectral density (LPSD) algorithm [25] (1000 frequencies, 100 averages) with 66.1 % overlapping BH92 windows [26].

have higher gradients in the spectral densities. For lower noise values the shape appears flat.

The noise floor of the data predominantly consists of the phasemeter readout noise, which is primarily dominated by ADC noise, shot noise, and RIN (for nonzero test mass tilts), as explained previously. However, it is worth mentioning that there is an unexplained percentage of the noise in the DWS data (see Ref. [7, Figure 23]).

We use the noise model described above for estimating the RIN level. We fit using a weighted Levenberg-Marquardt nonlinear least squares algorithm [28], invoking two free parameters: the RIN level $\tilde{r}$ and the phasemeter noise, parameterized by $\tilde{I}_{ADC}$.

F. Results and Discussion

Figure 9 represents the overall result of the average phase noise over the DWS "raw" phase, incorporating data from both experiments. All channels are combined, as they are expected to measure the same RIN. The plot illustrates two cases: the black (first experiment) and blue (second experiment) points in the plot correspond to the nominal case, where balanced detection is achieved using both output ports of the beam splitter; conversely, the green points (second experiment) indicate segments where one side of the phasemeter was disabled, resulting in the use of only one beam splitter output port; these segments are referred to as "unbalanced" since they lack balanced detection.

In addition, the plot includes noise model predictions (shown as solid lines for visibility) based on the results

of the fitting process, but the noise model is only evaluated at the points shown. After the fitting process, the segments have been sorted by DWS phase.

It is clear that the data from the first experiment (in black) is not consistent with the second experiment. This is likely due to an unknown change in noise levels that was observed during the time of the mission when this experiment was performed (see Fig. 4) and the different operating conditions a few hundred days apart. It still yields a result consistent with the generally expected pattern, but only samples a smaller parameter space below $\pi/2$, therefore not allowing the full model to be tested.

Upon examining the second experiment indicated by blue and green, several interesting aspects are visible. Primarily, the highest points of the sinusoidal RIN coupling show negligible variations between scenarios of balanced and unbalanced detection while still being consistent with zeros being at π, which suggests that $1f$-RIN was less than $2f$-RIN. This behavior is probably attributable to the analog power stabilization loop aboard LPF, aiming for a heterodyne frequency of 1 kHz, and experiencing gain reduction soon after (indicated by plots in proprietary mission documents, still well below requirements).

Second, the noise level around 0 rad increases by a factor of $\sqrt{2}$ when disabling balanced detection as anticipated. This amplification occurs because balanced detection results in a factor of $1/\sqrt{2}$ for uncorrelated noises (the combination of two correlated signals with two uncorrelated noise sources equals $\sqrt{2}/2$). Thus, the inverse situation arises when balanced detection is not in operation.
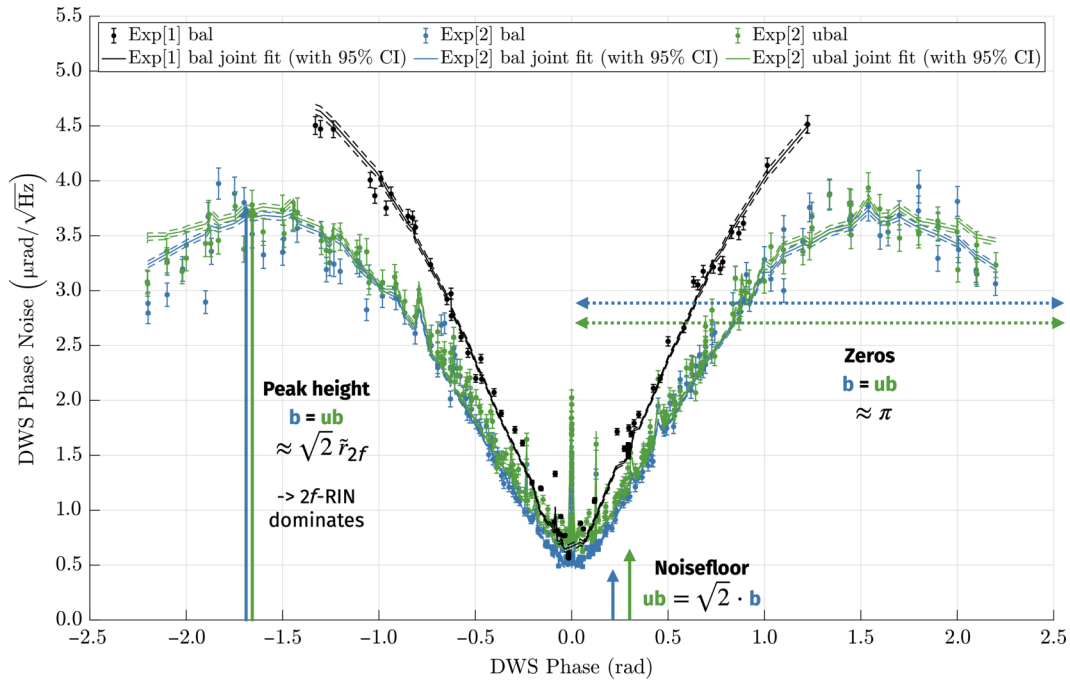
FIG. 9.   Results from both DWS tilt experiments. The black traces and points stem from the first investigation in June 2016 with smaller test mass tilts, whereas the remaining data are from the dedicated RIN experiment in February 2017. The annotations put the balanced "b" and unbalanced "ub" traces in relation. Here, $2f$-RIN is clearly dominant, since the peak heights remain approximately the same. For each experiment, all four DWS channels have been jointly analyzed, since they share the same RIN. The noise model differentiates between the angles, since it maps the data from the respective interferometers for each corresponding point. It has only been evaluated at the data points, and the solid lines are just plotted to improve visibility. Reanalyzed and modified with permission from Refs. [14,15].

Lastly, a number of points with enlarged noise levels are present around 0 rad. These instances occur when one DWS channel approaches zero offset (leading to vanishing RIN coupling), whereas its complementary channel maintains a nonzero offset (at increased RIN coupling). This condition implies a reduced contrast in X1 or X12 (depending on the specific test mass tilt), leading to higher noise coupling factors for the readout noises of the corresponding DWS channel of the same interferometer. This effects the channel that has vanishing RIN coupling most strongly, thus leading to the sharp increase around 0 rad.

In addition, a good number of points that do not exactly follow the standard sinusoidal RIN pattern match well with the data included in our model. This is related to the increase of phasemeter noise at lower contrasts. Around the peak points we see more variation than what our model predicted. This might be related to changes in how the laser was behaving over the course of the experiment, which lasted for 48 h.

For the second experiment the two free parameters estimated yield RIN (at $2f_{het}$) $\tilde{r} = 2.50(2) \times 10^{-6}/\sqrt{\text{Hz}}$ and ADC $\tilde{I}_{ADC} = 103.4(24) \times 10^{-12}$ pA/$\sqrt{\text{Hz}}$ with active balanced detection, and $\tilde{r} = 2.47(2) \times 10^{-6}/\sqrt{\text{Hz}}$, $\tilde{I}_{ADC} = 97.4(16) \times 10^{-12}$ pA/$\sqrt{\text{Hz}}$ with unbalanced detection. Confidence intervals for 95 % are plotted with dashed lines and corresponding colors. For the first experiment, the values are $\tilde{r} = 3.32(2) \times 10^{-6}/\sqrt{\text{Hz}}$ and ADC $\tilde{I}_{ADC} = 138.1(3) \times 10^{-12}$ pA/$\sqrt{\text{Hz}}$, with an increase in both RIN and phasemeter noise. The latter is not expected (see Ref. [7]) and remains unsolved.

With regards to the combined fitting approach chosen: this was selected because the X1 DWS channels exhibit substantially smaller tilts and fail to sample the majority of the RIN sinusoidal. Importantly, the RIN parameter is correlated between the DWS channels, whereas the ADC noise is not. This is particularly apparent as the anticipated $\sqrt{2}$ difference is well demonstrated in both the balanced and unbalanced cases.

The previously mentioned correlation between the ADC and RIN parameter is calculated from the fitting process, yielding a correlation coefficient of 0.35 (first experiment, balanced), 0.44 (second experiment, balanced), and 0.51 (second experiment, unbalanced). This strong correlation can be understood that when the test mass is tilted, it not only amplifies the RIN coupling strength because of an additional phase offset, but also modifies the contrast due to diminished beam overlap.

In terms of the contribution of $1f$-RIN during the unbalanced segments, it has not been incorporated into the model since it is indistinguishable in the data set.
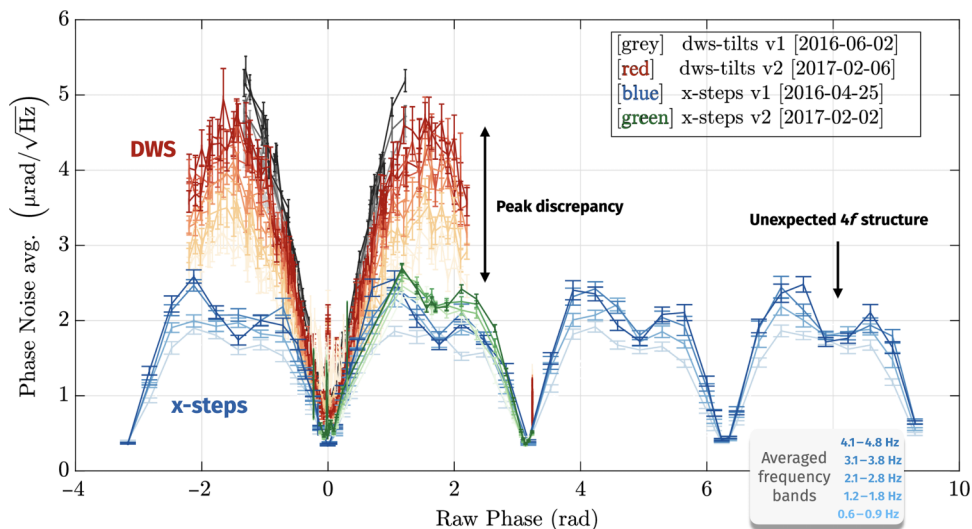
FIG. 10. Comparison of longitudinal and angular experiments for indirect RIN characterization for different frequency bands. Both x-steps and DWS tilts are analyzed for the same number of frequency bands for comparison (from lighter to darker color as stated in the bottom legend). It should be noted that the dip structure in blue was not observed in ground tests (see Ref. [5]) and the discrepancy remains unexplained thus far. Modified with permission from Ref. [15].

In summary, the phase-dependent noise coupling is confirmed in DWS, particularly by the findings of the second experiment, thereby verifying the theory of a sinusoidal systematic in the coupling. The duration allocated for each segment of measurement in this experiment was relatively short (less than 7 min as compared with more than 15 min in the first experiment). This was done to capture as many set points (approximately 60 per channel) as possible.

As suggested earlier by the unaltered maximum slope for both balanced and unbalanced detection scenarios, the $1f$-RIN appears to be significantly smaller than the $2f$-RIN. This aligns with the expectations drawn from ground measurements with the same active power control loop. As a result, the phase noise induced by RIN during the LPF mission is primarily dominated by $2f$-RIN, with only a minor contribution from $1f$-RIN.

In general, and for example in LISA, the opposite is expected. As the noise power in a band-limited spectrum tends to decrease towards higher frequencies, the $1f$-RIN coupling will be dominant most naturally, especially for higher heterodyne frequencies. Therefore, the coupling pattern without balanced detection is expected to rather follow the $1f$-dominated traces in Fig. 2 in general.

G. A systematic discrepancy observed in LPF flight data

The described method and results can be compared against data obtained from a similar experiment in the longitudinal data channel (so called "x-steps"), as outlined in the introduction. This was performed onground (see Ref. [5]) and twice inflight during the LPF mission at different times compared with the test mass tilts, see also

Ref. [12]. However, as Fig. 10 shows, especially the peak heights between angular and longitudinal channels do not agree, whereas the zeros around multiples of π appear to be consistent. The cause of this behavior remains unclear. However, both models show consistent fit results across both longitudinal and angular channels for data at the same time, as is evident from Figure 15 in Ref. [7]. That figure uses the data from experiment 2 of this article for a fit of the longitudinal model in the longitudinal channels. There, it confirms the same coupling strength in the differential o_{12} channel as we find in this article here within the errors, while utilizing the appropriate noise model. Therefore, the coupling model itself appears validated and the apparent factor two difference in the peak heights of Fig. 10 does not arise from the models themselves. Rather, the method of either "tilting" versus "stepping" may introduce roughly the factor two difference in the coupling, which could be related to a change in the overlap integral.

It should also be noted that in similar ground measurements the "$4f$" dip structure is not visible, as presented in Ref. [5]. More details on the discrepancy can be found in Ref. [15, Chapter 14].

We present this discrepancy also to encourage further ground-based experiments. For reference, there is ongoing effort to investigate noise couplings in DWS with the so-called TDOBS experiment [29].

VII. CONCLUSION

In this article, we have shown how laser RIN influences DWS measurements. This provides an indirect estimation of the RIN level $\tilde{r}$ to project its influence on angular and longitudinal phase channels, proving especially useful in

cases when no direct RIN measurements are available. This method is based on the inherent DWS common-mode rejection and can be considered complementary to a similar estimation via the longitudinal phase information, which, however, relies on an additional reference interferometer.

Measurements from the LPF space mission confirm the use-case, the expected coupling pattern and possible minimization around zero DWS phase offsets. The results are within mission requirements and corroborate the RIN estimates used in Refs. [6,7]. However, a factor-of-two discrepancy compared with similar longitudinal experiments appears in inflight data and fosters further research.

Moreover, the coupling and results presented in this article are directly applicable to LISA, where the local test mass interferometry is very similar to that on LPF. By design, due to the foreseen laser requirements and envisaged balanced detection, RIN is well mitigated in LISA, see also Ref. [19]. However, our introduced and tested scheme outlines a possible inflight characterization.

The research presented may also become applicable for future GRACE-FO style missions, if there is intent to implement a similar dragfree test mass with optical readout [30].

ACKNOWLEDGMENTS

[1] M. Colpi, K. Danzmann, M. Hewitson, K. Holley-Bockelmann, P. Jetzer, G. Nelemans, A. Petiteau, D. Shoemaker, C. Sopuerta, R. Stebbins *et al.*, LISA definition study report, arxiv:2402.07571.

[2] K. Abich, C. Braxmaier, M. Gohlke, J. Sanjuan, A. Abramovici, B. Bachman Okihiro, D. C. Barr, M. P. Bize, M. J. Burke, K. C. Clark *et al.*, In-orbit performance of the GRACE follow-on laser ranging interferometer, Phys. Rev. Lett. **123**, 031101 (2019).

[3] R. Stierlin, R. Bättig, P. D. Henchoz, and H. P. Weber, Excess-noise suppression in a fibre-optic balanced heterodyne detection system, Opt. Quantum Electron. **18**, 445 (1986).

[4] G. Hechenblaikner, Common mode noise rejection properties of amplitude and phase noise in a heterodyne interferometer, J. Opt. Soc. Am. A **30**, 941 (2013).

[5] L. Wissel, A. Wittchen, T. S. Schwarze, M. Hewitson, G. Heinzel, and H. Halloin, Relative-intensity-noise coupling in heterodyne interferometers, Phys. Rev. Appl. **17**, 024025 (2022).

[6] M. Armano, H. Audley, J. Baird, P. Binetruy, M. Born, D. Bortoluzzi, N. Brandt, E. Castelli, A. Cavalleri, A. Cesarini *et al.*, Sensor noise in LISA Pathfinder: In-flight performance of the optical test mass readout, Phys. Rev. Lett. **126**, 131103 (2021).

[7] M. Armano, H. Audley, J. Baird, P. Binetruy, M. Born, D. Bortoluzzi, N. Brandt, E. Castelli, A. Cavalleri, A. Cesarini *et al.*, Sensor noise in LISA Pathfinder: an extensive in-flight review of the angular and longitudinal interferometric measurement system, Phys. Rev. D **106**, 082001 (2022).

[8] E. Morrison, B. J. Meers, D. I. Robertson, and H. Ward, Experimental demonstration of an automatic alignment system for optical interferometers, Appl. Opt. **33**, 5037 (1994).

[9] E. Morrison, B. J. Meers, D. I. Robertson, and H. Ward, Automatic alignment of optical interferometers, Appl. Opt. **33**, 5041 (1994).

[10] G. Heinzel, M. D. Álvarez, A. Pizzella, N. Brause, and J. J. E. Delgado, Tracking length and differential-wavefront-sensing signals from quadrant photodiodes in heterodyne interferometers with digital phase-locked-loop readout, Phys. Rev. Appl. **14**, 054013 (2020).

[11] G. Wanner, G. Heinzel, E. Kochkina, C. Mahrdt, B. S. Sheard, S. Schuster, and K. Danzmann, Methods for simulating the readout of lengths and angles in laser interferometers with Gaussian beams, Opt. Commun. **285**, 4831 (2012).

[12] A. Wittchen, Relative Intensity Noise in the LISA Pathfinder Interferometer - Experiments on Ground and in Space, Ph.D. thesis, Hannover, 2021.

[13] L. Wissel, On behalf of the LPF collaboration, LISA Pathfinder: understanding DWS noise performance for the LISA mission, J. Phys.: Conf. Ser. **840**, 012044 (2017).

[14] L. Wissel, In-orbit performance and behaviour of the LISA Pathfinder Optical Metrology System, MA thesis, Leibniz Universität Hannover, 2017.

[15] L. Wissel, The Influence of Laser Relative Intensity Noise on Space-based Heterodyne Interferometers - from the LISA Pathfinder to the LISA Mission, PhD thesis, Leibniz University Hannover, 2024.

[16] G. Heinzel, *et al.*, *LPF final report for the German contribution to the nominal mission*, Tech. Rep. (Hannover, 2018).

[17] H. Audley, *et al.*, *LISA Pathfinder mission extension report for the German contribution*, Tech. Rep. (Hannover, 2020).

[18] G. Wanner and G. Heinzel, Analytical description of interference between two misaligned and mismatched complete Gaussian beams, Appl. Opt. **53**, 3043 (20140).

[19] L. Wissel, O. Hartwig, J. Bayle, M. Staab, E. Fitzsimons, M. Hewitson, and G. Heinzel, Influence of laser relative-intensity noise on the laser interferometer space antenna, Phys. Rev. Appl. **20**, 014016 (2023).

[20] M. Armano, H. Audley, G. Auger, J. T. Baird, M. Bassan, P. Binetruy, M. Born, D. Bortoluzzi, N. Brandt, M. Caleno *et al.*, Sub-Femto-g free fall for space-based gravitational

wave observatories: LISA Pathfinder results, Phys. Rev. Lett. **116** (2016).

[21] M. Armano, H. Audley, G. Auger, J. T. Baird, M. Bassan, P. Binetruy, M. Born, D. Bortoluzzi, N. Brandt, M. Caleno *et al.*, Beyond the required LISA free-fall performance: new LISA Pathfinder results down to 20 μHz, Phys. Rev. Lett. **120** (2018).

[22] M. Armano, H. Audley, J. Baird, P. Binetruy, M. Born, D. Bortoluzzi, E. Castelli, A. Cavalleri, A. Cesarini, V. Chiavegato *et al.*, In-depth analysis of LISA Pathfinder performance results: time evolution, noise projection, physical models, and implications for LISA, arXiv:2405.05207 [astro-ph.IM].

[23] M. Armano, H. Audley, J. Baird, P. Binetruy, M. Born, D. Bortoluzzi, E. Castelli, A. Cavalleri, A. Cesarini, A. M. Cruise *et al.*, Tilt-to-length coupling in LISA Pathfinder: a data analysis, Phys. Rev. D **108**, 102003 (2023).

[24] M. Armano, H. Audley, J. Baird, P. Binetruy, M. Born, D. Bortoluzzi, E. Castelli, A. Cavalleri, A. Cesarini, A. M. Cruise, K. Danzmann *et al.*, Tilt-to-length coupling in LISA Pathfinder: long-term stability, arXiv:2407.05852 [astro-ph.IM].

[25] M. Tröbs and G. Heinzel, Improved spectrum estimation from digitized time series on a logarithmic frequency axis, Measurement **39**, 120 (2006).

[26] G. Heinzel, A. Rüdiger, and R. Schilling, Spectrum and spectral density estimation by the discrete Fourier transform (DFT), including a comprehensive list of window functions and some new flat-top windows (2002).

[27] S. Vitale, *et al.*, Data series subtraction with unknown and unmodeled background noise, Phys. Rev. D **90**, 042003 (2014).

[28] G. Seber and C. Wild, *Nonlinear Regression*, Wiley Series in Probability and Statistics (Wiley, 2005).

[29] M. Chwalla, K. Danzmann, G. F. Barranco, E. Fitzsimons, O. Gerberding, G. Heinzel, C. J. Killow, M. Lieser, M. Perreur-Lloyd, D. I. Robertson *et al.*, Design and construction of an optical test bed for LISA imaging systems and tilt-to-length coupling, Classical Quantum Gravity **33**, 245015 (2016).

[30] A. Álvarez, A. Knudtson, U. Patel, J. Gleason, H. Hollis, J. Sanjuan, N. Doughty, G. McDaniel, J. Lee, J. Leitch *et al.*, A simplified gravitational reference sensor for satellite geodesy, J. Geod. **96** (2022).